Received: Added at production | Revised: Added at production | Accepted: Added at production

DOI: xxx/xxxx

ARTICLE TYPE

An unsymmetric 8-node plane element immune to mesh distortion for linear isotropic hardening material

Xiaotian Chen[1] | Wei Chen[1] | Jiangping Xu*[1] | Wenbin Tu[1] | Sellakkutti Rajendran*[2] | Jinzhong Lu[1]

[1]School of Mechanical Engineering, Jiangsu University, Zhenjiang, China
[2]School of Mechanical and Aerospace Engineering, Nanyang Technological University, Nanyang Avenue, Singapore

Correspondence
Jiangping Xu and Sellakkutti Rajendran, School of Mechanical Engineering, Jiangsu University, 301 Xuefu Road, Zhenjiang, Jiangsu Province, China and School of Mechanical and Aerospace Engineering, Nanyang Technological University Nanyang Avenue, 639798, Singapore. Email: jiangpingxu@ujs.edu.cn and msrajendran@ntu.edu.sg

Summary

An 8-node quadrilateral plane element US-QUAD8 is developed for linear isotropic hardening material in the framework of updated Lagrangian unsymmetric finite formulation where B_L matrix is constructed by classical shape function, and B_R matrix by the higher-order Lagrangian basis function in global coordinate system. The present element eliminates the influence of Jacobian in the elemental stiffness matrix and guarantees the quadratic completeness of displacement field even under severe distorted mesh. Two typical problems meshed with angular/curved-edge/mid-side distorted elements demonstrate excellent performance of distortion resistance of the present element and good computational efficiency in severe mesh distortion.

KEYWORDS:
unsymmetric finite element, material non-linearity, updated Lagrangian, large deformation, mesh distortion

1 | INTRODUCTION

Iso-parametric element has been able to provide reliable performance for regular meshes. However, its performance deteriorates dramatically or it encounters various locking problems [1,2,3] due to distorted mesh that can not be completely avoided in practice [4]. For simple geometry of computational domain, regular meshes without distortion can be easily obtained while distorted element cannot be completely avoided in case of complex geometry. Mesh distortion also occurs naturally during large deformation processes such as forging, extrusion, cutting and other fields [5,6,7]. To solve the problem caused by mesh distortion, commercial finite element analysis software adopts re-mesh strategy. However, the re-mesh technology involves much computation effort, especially for three dimensional (3D) complex structures. In addition, the automatic division of hexahedral mesh for 3D problem has not been solved completely. The second strategy is to use new analysis technologies that mesh conception is not included, such as FE-Meshfree method [8,9,10], material point method [11,12,13] and iso-geometric method [14,15,16,17,18]. In the present work, an unsymmeric 8-node element is developed to overcome the deteriorated results caused by mesh distortion in material non-linear problems.

Although the problem of mesh distortion has been known to researchers for decades, it is still an open question in finite element field. The conception of mesh distortion was first discovered in the 1970s [19,20,21]. Stricklin presented some results for a cantilever beam modelled with distorted and un-distorted elements and found that the 8-node iso-parametric elements (PP-QUAD8) performed badly when mesh was distorted [22]. Lee and Bathe attributed the decrease of accuracy caused by mesh distortion to the loss of polynomial completeness of shape functions in case of distorted element geometries [23]. The shape function loses its ability to accurately reproduce the Cartesian monomial terms in the displacement interpolation. Lautersztajn and Samuelsson found that by increasing the order of the displacement field interpolation function, the element performance

could be insensitive to certain types of mesh distortion[24]. This research led researchers to develop new elements capable of quadratic polynomial completeness in the global coordinate system.

Prathap et al. found that the absence of Jacobian in stiffness integral is a welcome feature because it helps to prevent mesh distortion effects from entering the element stiffness matrix through iso-parametric mapping of the element geometry[25]. In 2003, the unsymmetric finite element method proposed by Rajendran and Liew showed excellent performance in the case of severe mesh distortion in static analysis[26]. Under the linear bending problem, the 8-node unsymmetric finite element US-QUAD8 can obtain accurate solutions under three types of distortion mesh, such as angular distortion, mid-side node distortion and curved edge distortion. The unsymmetric finite element method was derived on the basis of Petrov-Galerkin formulation where test and trial functions are different. The test function is the standard iso-parametric interpolation function defined in the local coordinate system, which can meet the requirement of displacement continuity between elements. The trial function uses higher-order Lagrangian basis that meets the quadratic completeness of displacement interpolation in the global coordinate system. More importantly, the Jacobian determinant in the element stiffness matrix disappears. It directly avoids the influence of Jacobian determinant on element performance in case of mesh distortion. In one word, the unsymmetric finite element method includes three advantages: the continuity of the virtual displacement, the quadratic completeness of the real displacement and the elimination of the Jacobian. Ooi et al. extended the US-QUAD8 element to three dimensional US-HEXA20 solid element for geometric non-linear analysis[27,28]. The corresponding results showed better performance of US-HEXA20 than those obtained by classical element. By introducing the analytical trial function method, Cen et al. established a new unsymmetric finite element method that can overcome mesh distortion[29,30,31]. A series of related elements has been proposed by Cen and his co-workers, such as plane 4-node, 8-DOF quadrilateral element US-ATFQ4[32,33], 3D 8-node, 24-DOF hexahedral solid element US-ATFH8[34], the 8-node, 24-DOF hexahedral solid-shell element US-ATFHS8[35,36], and so on[37,38]. These novel unsymmetric elements have exhibited great advantages and showed excellent performance in case of anti-buckling edge distortion mesh and haven't brought significant additional computational effort. Although the developed distortion-immune elements have achieved great success in linear and geometric non-linear problems[39,40]. However, up to now, only few elements have been applied in material non-linear analysis to test their anti-distortion ability, such as US-ATFQ4 applied for hyperelastic analysis[41]. In the present work, US-QUAD8 element is extended into the framework of Updated Lagrangian (UL) formulation for linear isotropic hardening material and three typical mesh distortions as well as their combination are discussed.

The outline of this paper is as follows. In section 2, the unsymmetric formulation of US-QUAD8 element for linear isotropic hardening material problems is presented. In section 3, tip-moment and tip-shear examples with three types of mesh distortion as well as their combination are studied by the proposed method and important conclusions are summarized in section 4.

2 | UNSYMMETRIC FORMULATION FOR LINEAR ISOTROPIC HARDENING MATERIAL

Firstly, the shape functions of the classic PP-QUAD8 and US-QUAD8 elements are reviewed briefly. Then, the govern equations of the US-QUAD8 element for material non-linear problem are derived.

2.1 | The shape functions of the classical PP-QUAD8

In this section, we briefly recall the shape functions of the classical iso-parametric PP-QUAD8 element. The corresponding governing equation for linear problem is written as

$$\boldsymbol{K}\boldsymbol{U} = \boldsymbol{F} \tag{1}$$

where $\boldsymbol{U}$ is the nodal displacement vector and $\boldsymbol{F}$ is the load vector. The global stiffness matrix, $\boldsymbol{K}$, is written as

$$\boldsymbol{K} = \int_{\Omega} \boldsymbol{B}^T \boldsymbol{D} \boldsymbol{B} d\Omega \tag{2}$$

where $\boldsymbol{B}$ is the element strain-displacement matrix, $\boldsymbol{D}$ is the constitutive matrix and Ω is the computational domain. Usually, $\boldsymbol{B}$ is constructed by using the classical 8-node iso-parametric shape functions

$$N_i = \frac{1}{4}\left(1+\xi\xi_i\right)\left(1+\eta\eta_i\right)\left(\xi\xi_i+\eta\eta_i-1\right) \tag{3}$$

$$N_j = \frac{1}{2}\left(1-\xi^2\right)\left(1+\eta\eta_j\right) \tag{4}$$

$$N_k = \frac{1}{2}\left(1+\xi\xi_k\right)\left(1-\eta^2\right) \tag{5}$$

where i, j and k refer to corner nodes, mid-side nodes along ξ=0 edges, and mid-side nodes along η=0 edges, respectively. The shape function matrix is defined as

$$\boldsymbol{N} = \begin{bmatrix} N_1 & 0 & N_2 & 0 & N_3 & 0 & \cdots & N_8 & 0 \\ 0 & N_1 & 0 & N_2 & 0 & N_3 & \cdots & 0 & N_8 \end{bmatrix} \tag{6}$$

where N_i is the shape function at element node i and $\boldsymbol{B}$ matrix is given by

$$\boldsymbol{B} = \begin{bmatrix} \frac{\partial N_1}{\partial x} & 0 & \frac{\partial N_2}{\partial x} & 0 & \cdots \\ 0 & \frac{\partial N_1}{\partial y} & 0 & \frac{\partial N_2}{\partial y} & \cdots \\ \frac{\partial N_1}{\partial y} & \frac{\partial N_1}{\partial x} & \frac{\partial N_2}{\partial y} & \frac{\partial N_2}{\partial x} & \cdots \end{bmatrix} \tag{7}$$

where $\partial N_i/\partial x$ and $\partial N_i/\partial y$ are the derivatives of shape functions with respect to x and y, respectively.

$$\begin{Bmatrix} \frac{\partial N_i}{\partial x} \\ \frac{\partial N_i}{\partial y} \end{Bmatrix} = \boldsymbol{J}^{-1} \begin{Bmatrix} \frac{\partial N_i}{\partial \xi} \\ \frac{\partial N_i}{\partial \eta} \end{Bmatrix} = \frac{\mathrm{Adj}[\boldsymbol{J}]}{|\boldsymbol{J}|} \begin{Bmatrix} \frac{\partial N_i}{\partial \xi} \\ \frac{\partial N_i}{\partial \eta} \end{Bmatrix} \tag{8}$$

where Adj[$\boldsymbol{J}$] is adjugate matrix of $\boldsymbol{J}$ and $|\boldsymbol{J}|$ is the determinant of Jacobian matrix. So we can replace the strain-displacement matrix with $\boldsymbol{B} = \boldsymbol{B}^*/|\boldsymbol{J}|$. $\boldsymbol{B}^*$ is the adjoint matrix of $\boldsymbol{B}$. And then, the elemental stiffness matrix $\boldsymbol{K}^e$ is rewritten as

$$\boldsymbol{K}^e = \int_{\Omega^e} \boldsymbol{B}^T \boldsymbol{D}\boldsymbol{B} d\Omega^e = \int_{-1}^{1}\int_{-1}^{1} \frac{\left(\boldsymbol{B}^*\right)^T}{|\boldsymbol{J}|} \boldsymbol{D} \frac{\left(\boldsymbol{B}^*\right)}{|\boldsymbol{J}|} |\boldsymbol{J}| t d\xi d\eta = \int_{-1}^{1}\int_{-1}^{1} \frac{\left(\boldsymbol{B}^*\right)^T}{|\boldsymbol{J}|} \boldsymbol{D}\boldsymbol{B}^* t d\xi d\eta \tag{9}$$

where t is the thickness of the object and Ω^e is the elemental domain. It can be observed that the $|\boldsymbol{J}|$ is included in the integrand of the element stiffness matrix. When the element shape is regular, the value of $|\boldsymbol{J}|$ is constant, but when the element shape is irregular, the Jacobi changes and is hard to integrate accurately. In addition, when the $|\boldsymbol{J}|$ in the denominator is equal to zero after mesh distortion, the element stiffness matrix cannot be integrated.

2.2 | The shape function of the unsymmetric element

The classical iso-parametric element displacement field could be written as

$$\begin{aligned} u &= \alpha_1 + \alpha_2\xi + \alpha_3\eta + \alpha_4\xi^2 + \alpha_5\xi\eta + \alpha_6\eta^2 + \alpha_7\xi^2\eta + \alpha_8\xi\eta^2 \\ v &= \beta_1 + \beta_2\xi + \beta_3\eta + \beta_4\xi^2 + \beta_5\xi\eta + \beta_6\eta^2 + \beta_7\xi^2\eta + \beta_8\xi\eta^2 \end{aligned} \tag{10}$$

where α_i and β_i are parameters to be determined. When the mesh is regular, the displacement field of classical element is quadratic complete in both local and global coordinate systems. But when the mesh is distorted, only the linear completeness of the displacement field is guaranteed in the global coordinate system. Therefore, in order to improve the performance of the element, it is necessary to construct a new shape function to ensure the quadratic completeness of displacement field in the global coordinate system under any meshes. Firstly, we write the displacement field as

$$\begin{aligned} u(x,y) &= a_1 + a_2x + a_3y + a_4x^2 + a_5xy + a_6y^2 + a_7x^2y + a_8xy^2 \\ v(x,y) &= b_1 + b_2x + b_3y + b_4x^2 + b_5xy + b_6y^2 + b_7x^2y + b_8xy^2 \end{aligned} \tag{11}$$

where a_i and b_i are parameters to be determined. To satisfy the quadratic completeness in the global coordinate system, a new form function M_i based on a Lagrangian higher-order interpolation basis function is adopted to ensure the quadratic

completeness. M_i is solved by equation (12)

$$\begin{bmatrix} 1 & 1 & 1 & 1 & 1 & 1 & 1 & 1 \\ x_{1-c} & x_{2-c} & x_{3-c} & x_{4-c} & x_{5-c} & x_{6-c} & x_{7-c} & x_{8-c} \\ y_{1-c} & y_{2-c} & y_{3-c} & y_{4-c} & y_{5-c} & y_{6-c} & y_{7-c} & y_{8-c} \\ x_{1-c}^2 & x_{2-c}^2 & x_{3-c}^2 & x_{4-c}^2 & x_{5-c}^2 & x_{6-c}^2 & x_{7-c}^2 & x_{8-c}^2 \\ x_{1-c}y_{1-c} & x_{2-c}y_{2-c} & x_{3-c}y_{3-c} & x_{4-c}y_{4-c} & x_{5-c}y_{5-c} & x_{6-c}y_{6-c} & x_{7-c}y_{7-c} & x_{8-c}y_{8-c} \\ y_{1-c}^2 & y_{2-c}^2 & y_{3-c}^2 & y_{4-c}^2 & y_{5-c}^2 & y_{6-c}^2 & y_{7-c}^2 & y_{8-c}^2 \\ x_{1-c}^2y_{1-c} & x_{2-c}^2y_{2-c} & x_{3-c}^2y_{3-c} & x_{4-c}^2y_{4-c} & x_{5-c}^2y_{5-c} & x_{6-c}^2y_{6-c} & x_{7-c}^2y_{7-c} & x_{8-c}^2y_{8-c} \\ x_{1-c}y_{1-c}^2 & x_{2-c}y_{2-c}^2 & x_{3-c}y_{3-c}^2 & x_{4-c}y_{4-c}^2 & x_{5-c}y_{5-c}^2 & x_{6-c}y_{6-c}^2 & x_{7-c}y_{7-c}^2 & x_{8-c}y_{8-c}^2 \end{bmatrix} \begin{Bmatrix} M_1 \\ M_2 \\ M_3 \\ M_4 \\ M_5 \\ M_6 \\ M_7 \\ M_8 \end{Bmatrix} = \begin{Bmatrix} 1 \\ x_{-c} \\ y_{-c} \\ x_{-c}^2 \\ x_{-c}y_{-c} \\ y_{-c}^2 \\ x_{-c}^2y_{-c} \\ x_{-c}y_{-c}^2 \end{Bmatrix} \tag{12}$$

and

$$\left.\begin{aligned} x_{i-c} &= x_i - x_c \\ y_{i-c} &= y_i - y_c \\ x_{-c} &= x - x_c \\ y_{-c} &= y - y_c \end{aligned}\right\}, \quad i = 1, 2, 3, \ldots, 8 \tag{13}$$

where (x_c, y_c) is the centroid of the element, M_i is obtained by solving the completeness conditions themselves. The shape function matrix is then defined as

$$\boldsymbol{M} = \begin{bmatrix} M_1 & 0 & M_2 & 0 & M_3 & 0 & \cdots & M_8 & 0 \\ 0 & M_1 & 0 & M_2 & 0 & M_3 & \cdots & 0 & M_8 \end{bmatrix} \tag{14}$$

B_R matrix is given by

$$\boldsymbol{B}_R = \begin{bmatrix} \frac{\partial M_1}{\partial x} & & \frac{\partial M_i}{\partial x} & \\ & \frac{\partial M_1}{\partial y} & \cdots & \frac{\partial N_i}{\partial y} & \cdots \\ \frac{\partial M_1}{\partial y} & \frac{\partial M_1}{\partial x} & \frac{\partial M_i}{\partial y} & \frac{\partial M_i}{\partial x} & \end{bmatrix} \tag{15}$$

Based on the unsymmetric finite element method[26,42], two different $\boldsymbol{B}$ matrices are constructed by different shape functions and the $\boldsymbol{K}^e$ is rewritten as

$$\boldsymbol{K}^e = \int_{\Omega^e} \boldsymbol{B}_L^T \boldsymbol{D} \boldsymbol{B}_R d\Omega^e = \int_{-1}^{1}\int_{-1}^{1} \frac{\left(\boldsymbol{B}^*\right)^T}{|\boldsymbol{J}|} \boldsymbol{D} \boldsymbol{B}_R |\boldsymbol{J}| t d\xi d\eta = \int_{-1}^{1}\int_{-1}^{1} \left(\boldsymbol{B}^*\right)^T \boldsymbol{D} \boldsymbol{B}_R t d\xi d\eta \tag{16}$$

Equation (16) satisfies the requirement of the quadratic completeness in the global coordinate system. Also, using of the two different shape functions eliminates the $|\boldsymbol{J}|$ which is affected by mesh distortion. It is a good property for the element to be immune to mesh distortions. Readers are referred to[42] for more details.

2.3 | Framework of the US-QUAD8 element for linear isotropic hardening material

Updated Lagrangian formulation is adopted in the US-QUAD8 element for material non-linear analysis[43]. There are three different configurations of the body in the formulation, namely the initial un-deformed configuration C_0, the last known configuration C_1 in the previous time step and the unknown configuration in the current time step C_2. The updated Lagrangian algorithm can be obtained by virtual work principle

$$\delta W = \int_{{}^2\Omega} {}^2\sigma_{ij} \delta \left({}_2e_{ij}\right) d^2\Omega - \int_{{}^2\Omega} {}^2f_i \delta u_i d^2\Omega - \int_{{}^2\Gamma} {}^2t_i \delta u_i d^2\Gamma = 0 \tag{17}$$

where ${}^2\sigma_{ij}$ is Cauchys stress tensor, ${}_2e_{ij}$ is the infinitesimal strain tensor and δu_i is the virtual displacement components. ${}^2f_i$ and ${}^2t_i$ are the body force and boundary traction components in configuration C_2. However, C_2 is unknown, so the equation (17) is rewritten based on C_1

$$\delta W = \int_{{}^1\Omega} {}^2_1S_{ij} \delta \left({}^2_1\varepsilon_{ij}\right) d^1\Omega - \int_{{}^1\Omega} {}^2_1f_i \delta u_i d^1\Omega - \int_{{}^1\Gamma} {}^2_1t_i \delta u_i d^1\Gamma = 0 \tag{18}$$

${}^2_1 f_i$ and ${}^2_1 t_i$ are the body force and boundary traction components referred to the configuration C_1. ${}^2_1 S_{ij}$ is the updated second Piola-Kirchhoff stress tensor and ${}^2_1 \varepsilon_{ij}$ is the updated Green-Lagrange strain tensor measured from C_1 to C_2. ${}^2_1 S_{ij}$ is written as

$$ {}^2_1 S_{ij} = {}^1\sigma_{ij} + {}_1 S_{ij} \tag{19} $$

and ${}^2_1 \varepsilon_{ij}$ is given by

$$ {}^2_1 \varepsilon_{ij} = \frac{1}{2}\left(\frac{\partial u_i}{\partial {}^1 x_j} + \frac{\partial u_j}{\partial {}^1 x_i} + \frac{\partial u_k}{\partial {}^1 x_i}\frac{\partial u_k}{\partial {}^1 x_j} \right) \equiv {}^1 e_{ij} + {}^1\eta_{ij} \tag{20} $$

where ${}^1\sigma_{ij} \equiv {}^1_1 S_{ij}$ is the Cauchy stress tensor in configuration C_1 and ${}_1 S_{ij}$ is the updated Kirchhoff stress increment tensor. ${}^1 e_{ij}$ and ${}^1\eta_{ij}$ are the linear and nonlinear incremental strains referred to configuration C_1, respectively. Substitute Eqs. (19) and (20) into Eq. (18), the governing formula is written as follows:

$$ \int_{{}^1\Omega} \boldsymbol{B}_L^T \boldsymbol{D}_T \boldsymbol{B}_R d^1\Omega \boldsymbol{U} = \int_{{}^1\Omega} \boldsymbol{N}^T {}^2_1\boldsymbol{f} d^1\Omega + \int_{{}^1\Gamma} \boldsymbol{N}^T {}^2_1\boldsymbol{t} d^1\Gamma - \int_{{}^1\Omega} \boldsymbol{B}_L^T \left\{ {}^1\sigma \right\} d^1\Omega \tag{21} $$

Where $\boldsymbol{U}$ is the nodal displacement increment vector Equation (21) can be simplified by dropping the geometrical nonlinear term

$$ \boldsymbol{K}\boldsymbol{U} = {}^2_1\boldsymbol{F} - {}^1_1\boldsymbol{F} \tag{22} $$

Following the steps provided in book[44], the material tangent stiffness matrix $\boldsymbol{D}_T = \partial\Delta\boldsymbol{\sigma}/\partial\Delta\boldsymbol{\epsilon}$ is determined for Newton Raphson method to solve the Eq. (22). In the present work, the external force is added step by step. In each load step, the increment in stress is calculated as follows

$$ {}_1 S = \Delta\boldsymbol{\sigma} = 2G\Delta\epsilon^e + \lambda \boldsymbol{I}\Delta\epsilon^e : \boldsymbol{I} \tag{23} $$

where $\boldsymbol{G}$ and λ are the shear modulus and Lame constant, respectively. $\boldsymbol{I}$ is the identity tensor and the symbol : is double contraction. The elastic strain increment is updated according to $\Delta\epsilon^e = \Delta\epsilon - \Delta\epsilon^p$. An implicit integration scheme with a plastic correction is adopted to avoid stress draft from Mises yield surface[44]. With the technology called radial return method, the plastic strain increment $\Delta\epsilon^p$ is obtained and then the elastic strain increment is calculated through the total strain $\Delta\epsilon$. The quantities in equation (22) are expressed as below

$$ \left\{ {}^1\sigma \right\} = \left\{ {}^1\sigma_{xx} \; {}^1\sigma_{yy} \; {}^1\sigma_{xy} \right\}^T \tag{24} $$

$$ \boldsymbol{B}_L = \begin{bmatrix} \frac{\partial N_1}{\partial {}^1 x} & 0 & \frac{\partial N_2}{\partial {}^1 x} & 0 & \cdots \\ 0 & \frac{\partial N_1}{\partial {}^1 y} & 0 & \frac{\partial N_2}{\partial {}^1 y} & \cdots \\ \frac{\partial N_1}{\partial {}^1 y} & \frac{\partial N_1}{\partial {}^1 x} & \frac{\partial N_2}{\partial {}^1 y} & \frac{\partial N_2}{\partial {}^1 x} & \cdots \end{bmatrix} \quad \boldsymbol{B}_R = \begin{bmatrix} \frac{\partial M_1}{\partial {}^1 x} & 0 & \frac{\partial M_2}{\partial {}^1 x} & 0 & \cdots \\ 0 & \frac{\partial M_1}{\partial {}^1 y} & 0 & \frac{\partial M_2}{\partial {}^1 y} & \cdots \\ \frac{\partial M_1}{\partial {}^1 y} & \frac{\partial M_1}{\partial {}^1 x} & \frac{\partial M_2}{\partial {}^1 y} & \frac{\partial M_2}{\partial {}^1 x} & \cdots \end{bmatrix} \tag{25} $$

$$ {}^2_1\boldsymbol{F} = \int_{{}^1\Omega} \boldsymbol{N}^T {}^2_1\boldsymbol{f} d^1\Omega + \int_{{}^1\Gamma} \boldsymbol{N}^T {}^2_1\boldsymbol{t} d^1\Gamma \tag{26} $$

$$ {}^1_1\boldsymbol{F} = \int_{{}^1\Omega} \boldsymbol{B}_L^T \left\{ {}^1\sigma \right\} d^1\Omega \tag{27} $$

3 | NUMERICAL EXAMPLES

For comparison purpose, two typical elements are briefly introduced below.

(1) PP-QUAD8: This is the classical iso-parametric symmetric 8-node quadrilateral element and widely used in ANSYS. This element uses the same $\boldsymbol{B}_L$ matrix on the left and right side of the tangent matrix $\boldsymbol{D}_T$ in the stiffness integral. The prefix PP here signifies that the $\boldsymbol{B}_L$ is constructed by parametric shape function. The element stiffness matrix is given as

$$ \boldsymbol{K}^e = \int_{-1}^{1}\int_{-1}^{1} \boldsymbol{B}_L^T \boldsymbol{D}_T \boldsymbol{B}_L |\boldsymbol{J}| t d\xi d\eta \tag{28} $$

(2) US-QUAD8: This element uses the different $\boldsymbol{B}$ matrix in the integral of the stiffness matrix. The prefix US signifies that $\boldsymbol{B}_L$ and $\boldsymbol{B}_R$ matrices are obtained by parametric and metric shape functions, respectively. The element stiffness matrix is given as

$$\boldsymbol{K}^e = \int_{-1}^{1}\int_{-1}^{1} \boldsymbol{B}_L^T \boldsymbol{D}_T \boldsymbol{B}_R t d\xi d\eta \tag{29}$$

In order to assess the performance of the classical and present elements under mesh distortion, three different types of geometric distortion as well as severe distortion are considered. Based on the classification of Lee and Bathe[23], there are three different types of distortion associated with the quadrilateral plane elements, namely angular distortion, curved-edge distortion and mid-side node distortion shown in Fig. 1. Angular distortion occurs most frequently in the transition regions from sparse to intensive meshes, next to the complicated boundaries, or is generated by automatic mesh algorithm which are usually unavoidable[23]. Especially in non-linear large deformation problems, serious angular distortion happens commonly. Curved-edge distortion also occurs very frequently when fit a curved boundary. It also appears when an initially straight edge becomes curved in large deformation[23]. In the following tests, cantilever beams subjected to tip moment and shear loads are analysed and the above three mesh distortions and mixed distortion are applied in the initial meshes to compare the performance of the two elements immunity to distortion for material non-linear problems. All the objects are meshed with four elements.

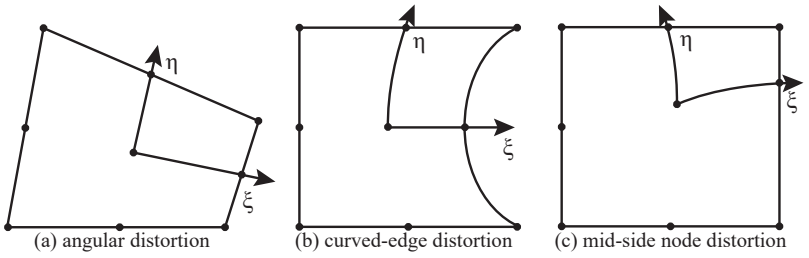

FIGURE 1 Three different types of mesh distortion

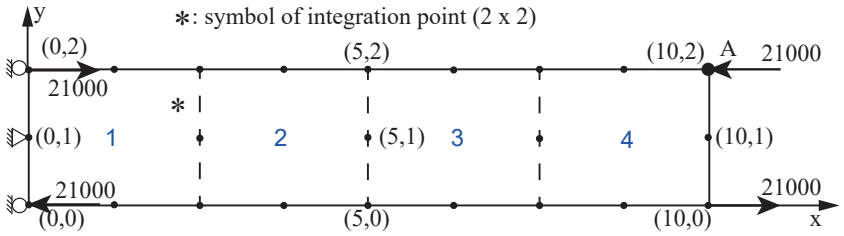

FIGURE 2 A tip-moment cantilever beam model with a regular mesh. The following material parameters and beam sizes are used in this example. $E = 5 \times 10^6$ Pa , $\upsilon = 0.25$, $\sigma_y = 900$ Pa and $h = 50000$ Pa, length of the beam $l = 10$ m, width $w = 2$ m, depth $t = 2$ m. 2×2 Gaussian integration scheme is used.

3.1 | A cantilever beam with a moment load

A cantilever beam subjected to a tip moment involves a quadratic displacement field and hence is a good problem to test the mesh distortion sensitivity of a quadratic element. The specific model and material properties are shown in Fig. 2. The moment force is distributed by applying equivalent nodal forces of -21000 N and 21000 N at points $(10, 2)$ and $(10, 0)$, respectively. The reaction moment force at the fixed end is represented by 21000 N and -21000 N at points $(0, 2)$ and $(0, 0)$, respectively. Material

parameters and beam sizes are given as $E = 5 \times 10^6$ Pa , $\upsilon = 0.25$, $\sigma_y = 900$ Pa and $h = 50000$ Pa, length of the beam $l = 10$ m, width $w = 2$ m, depth $t = 2$ m. All the examples in this sub-section use the same material parameters.

In case of regular mesh, the contour plots of σ_{xx} stress and the effective plastic strain obtained by the two elements are shown in Fig. 3. The contour lines of the σ_{xx} stress and the effective plastic strain appear smooth and continuous across the element boundaries. PP-QUAD8 and US-QUAD8 both reproduce good stress distributions when the elements are regular. The maximum and minimum σ_{xx} stresses are 21248 Pa and −21248 Pa, respectively. The maximum and minimum effective plastic strains are 0.276 and 0, respectively.

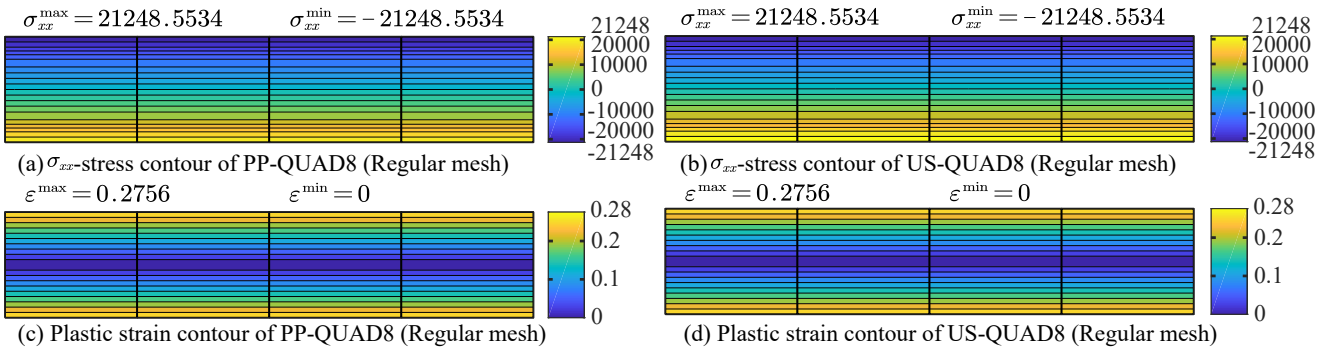

FIGURE 3 Contours of σ_{xx} stress and effective plastic strain for the tip-moment cantilever beam with regular mesh are plotted on the undeformed meshes

The curves of vertical displacement at point A and the σ_{xx} stress at the fourth Gaussian integration point (see Fig. 2) in the first element versus the load step are shown in Fig. 4. Obviously, the displacement undergoes two stages: linear static (load steps from 0 to 20) and material nonlinear stages (load steps from 20 to 200). When the elements are regular, the curves of displacement and stress at integration point for PP-QUAD8 and US-QUAD8 are identical. The maximum vertical displacement is 12.268 m. The σ_{xx} stress of the fourth integration point is −10600.151 Pa.

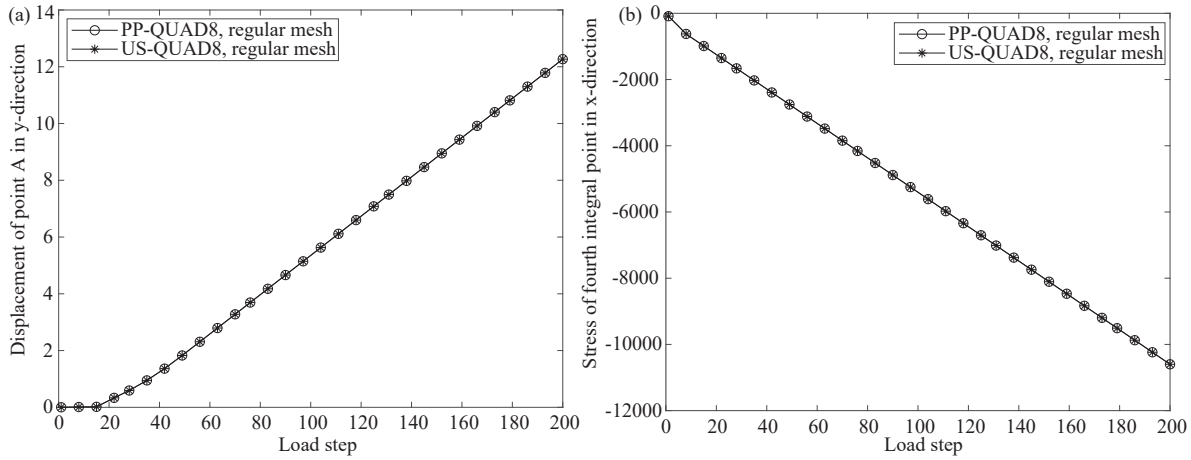

FIGURE 4 (a) Curves of vertical displacement at point A and (b) σ_{xx} stress at the fourth integration point in the first element versus the load step in cases of regular mesh

3.1.1 | Single distortion

Three kinds of single distortions plotted in Fig. 5 have been used to verify the performance of this two elements. The coordinates of nodes with this three different types of distortion are given as follows. The nodes with angular distortion are node 18 (3, 2), node 19 (1.5, 2), node 17 (4.25, 2), node 15 (6.75, 2), node 13 (9, 2), node 3 (1, 0), node 5 (3.25, 0), node 7 (5.75, 0), node 9 (8.5, 0), node 16 (5.5, 2), node 14 (8, 2), node 4 (2, 0), node 6 (4.5, 0), node 8 (7, 0) and with curved-edge distortion are node 21 (1.8, 1), node 22 (4.3, 1) and node 23 (6.8, 1). For mid-side node distortion, the distorted nodal coordinates are node 19 (0.65, 2), node 17 (3.15, 2), node 15 (5.65, 2), node 13 (8.15, 2), node 3 (1.25, 0), node 5 (3.75, 0), node 7 (6.25, 0) and node 9 (8.75, 0).

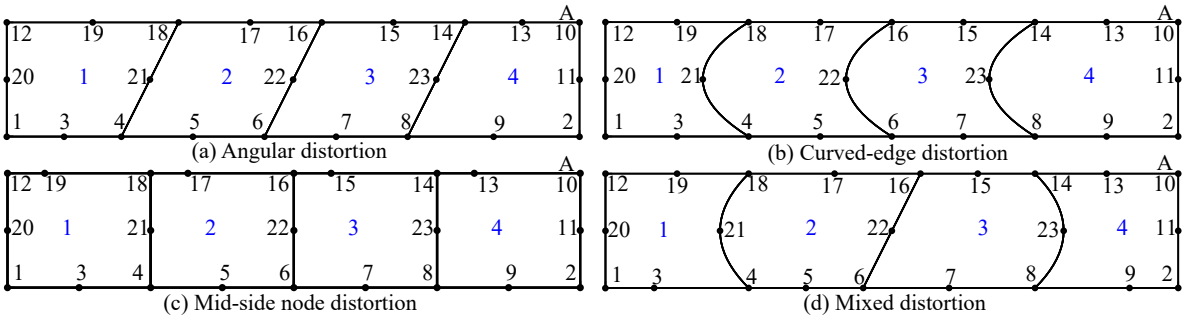

FIGURE 5 Different types of distortion meshes for the tip-moment cantilever beam

From the contour plots in Fig. 6, US-QUAD8 reproduces exact σ_{xx} stress distributions in the three distortion cases which are consistent with that obtained from regular mesh, while the PP-QUAD8 reproduces bad results. The maximum σ_{xx} stress and effective plastic strain for US-QUAD8 are 21248.553 Pa and 0.28 which are the same as those in case of regular mesh. However, for PP-QUAD8 element, the stress contours and effective plastic strain are lack of continuity and smoothness. The distribution of effective plastic strain for PP-QUAD8 seems similar with US-QUAD8 element, see Figs. 6(c) and (d). Adjustment of the maximum and minimum values in the colour bar for being equal to those in US-QUAD8 makes the plot more worse. So we leave them as original values. The maximum σ_{xx} stresses for PP-QUAD8 are 63907.850 Pa, 555284.657 Pa and 463669.667 Pa in the three cases of single distorted mesh. The corresponding relative errors of σ_{xx} stress are 200.763%, 2513.282% and 2082.123% comparing with the corresponding results in case of regular mesh. Table 1 lists the relative errors of maximum σ_{xx} stress in the whole domain, displacement at point A in y direction and σ_{xx} stress at the fourth Gaussian point in the first element. The corresponding reference values are from those in case of regular mesh.

TABLE 1 Relative errors in case of tip moment example

Element type \ Distortion type	Angular distortion	Curved-edge distortion	Mid-side node distortion	Mixed distortion
PP-QUAD8 (σ_{xx})	200.763%	2513.282%	2082.123%	–
US-QUAD8 (σ_{xx})	**0%**	**0%**	**0%**	**0%**
PP-QUAD8 (U)	0.953%	7.829%	6.845%	–
US-QUAD8 (U)	**0%**	**0%**	**0%**	**0%**
PP-QUAD8 (σ_{xx}^{gp})	0.151%	5.884%	5.043%	–
US-QUAD8 (σ_{xx}^{gp})	**0%**	**0%**	**0%**	**0%**

U: the displacement at point A in y direction
σ_{xx}^{gp}: the stress at the fourth Gaussian point in the first element
-: cannot converge

The graphs of vertical displacement and σ_{xx} stress at the fourth integration point in the first element are plotted in Fig. 7. As can be seen from the graphs, the curves of displacement and σ_{xx} stress at integration point for PP-QUAD8 both deviate from the exact result in cases of curved-edge distortion and mid-side node distortion. Although, there is little difference between the two elements in the case of angular distortion, but the distribution of σ_{xx} stress for US-QUAD8 is much better than PP-QUAD8 and

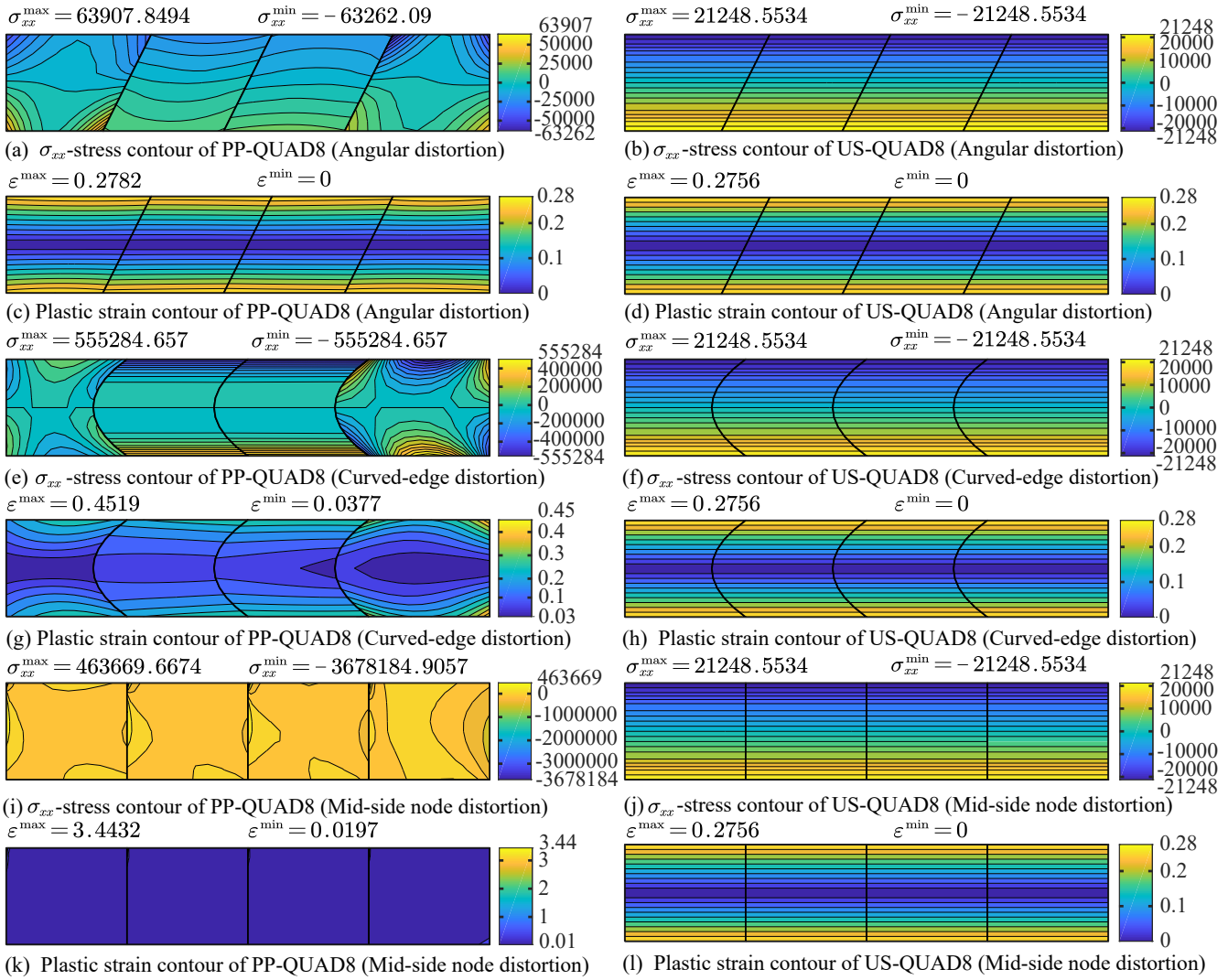

FIGURE 6 Contours of σ_{xx} stress and effective plastic strain for the tip-moment cantilever beam with angular distortion, curved-edge distortion and mid-side node distortion are plotted on the undeformed meshes

is comparable with that in case of regular mesh. The maximum vertical displacements for PP-QUAD8 are 12.151 m, 11.308 m, 11.429 m, respectively, in the three distortion cases and are all 12.268 m for US-QUAD8 which is same as that in regular mesh. The maximum σ_{xx} stresses at integration point for PP-QUAD8 are -10584.112 Pa, -9976.416 Pa, -10065.567 Pa, respectively, and for US-QUAD8 are all 10600.151 Pa which is identical with that in regular mesh.

3.1.2 | Mixed distortion

An extremely distorted mesh has been used to test the distortion resistance of the US-QUAD8 element in material non-linearity. The extremely distorted mesh is complex since it combines the three single distortions mentioned above and plotted in Fig. 5(d). The distorted nodes are node 3 $(0.85, 2)$, node 21 $(2, 1)$, node 17 $(4, 2)$, node 16 $(5.5, 2)$, node 6 $(4.5, 0)$, node 5 $(3.5, 0)$, node 7 $(6, 0)$, node 15 $(6.5, 2)$, node 23 $(8, 1)$ and node 9 $(9.15, 0)$.

As shown in Fig. 8, US-QUAD8 reproduces exact σ_{xx} stress and effective plastic contours. In this severe distortion, the PP-QUAD8 cannot converge after the $18th$ load step while US-QUAD8 can converge at the final load step 200. In addition, the contour lines of σ_{xx} stress (Fig. 8) and effective plastic strain for PP-QUAD8 are really bad. However, the corresponding contour lines for US-QUAD8 are smooth and continuous across the element boundaries and the same as those obtained in case of regular

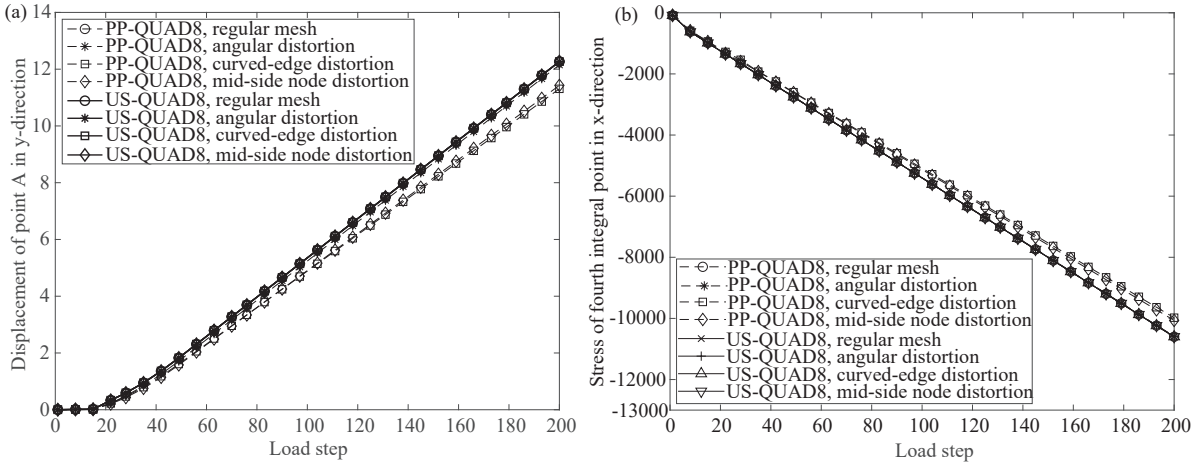

FIGURE 7 (a) Curves of vertical displacement at point A and (b) the σ_{xx} stress at the fourth integration point in the first element versus the load step in cases of single distortion. The curves of US-QUAD8 are consistent with that of PP-QUAD8 under regular mesh.

mesh. As the graphs shown in Fig. 9, the curves of vertical displacement and σ_{xx} stress at Gaussian point for PP-QUAD8 can only converge to $18th$ load step.

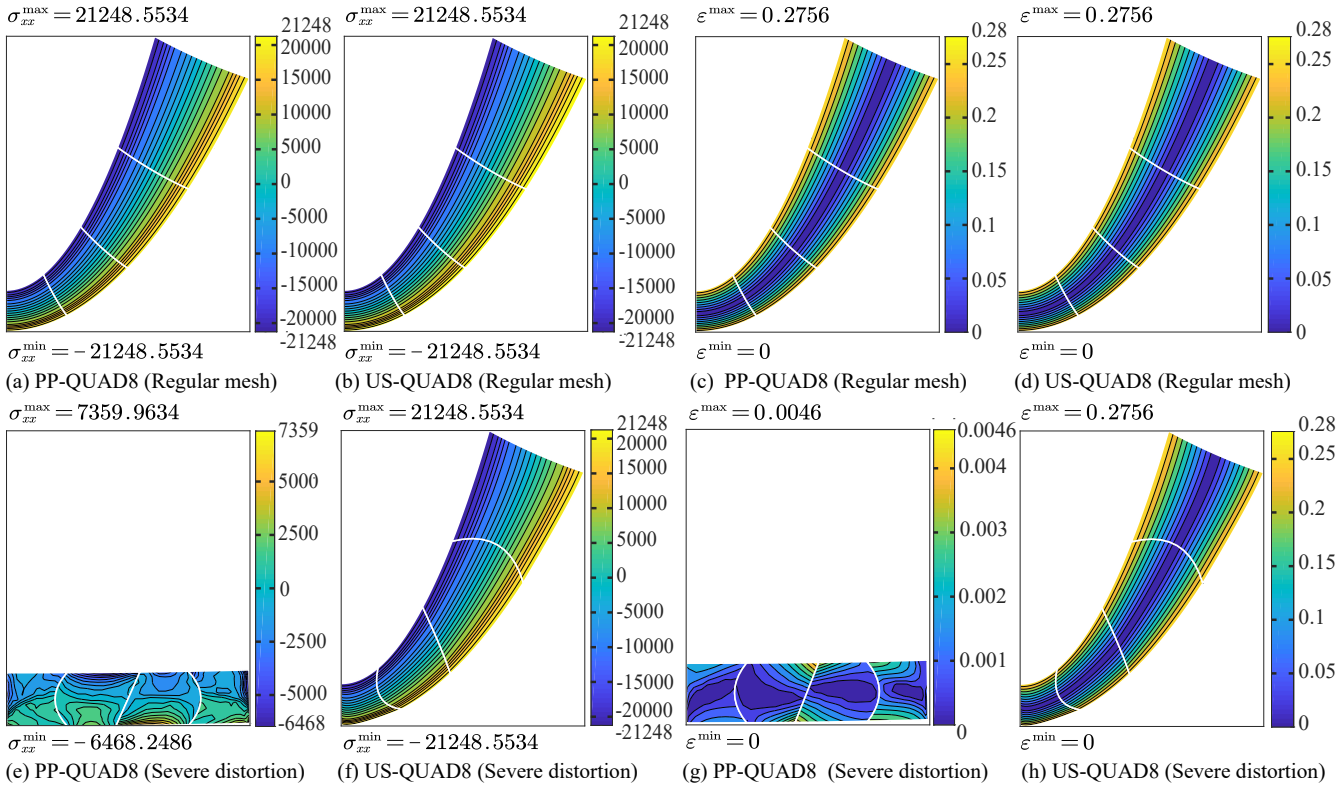

FIGURE 8 Contours of σ_{xx} stress and effective plastic strain for the tip-moment cantilever beam with mixed distortion are plotted on the deformed meshes

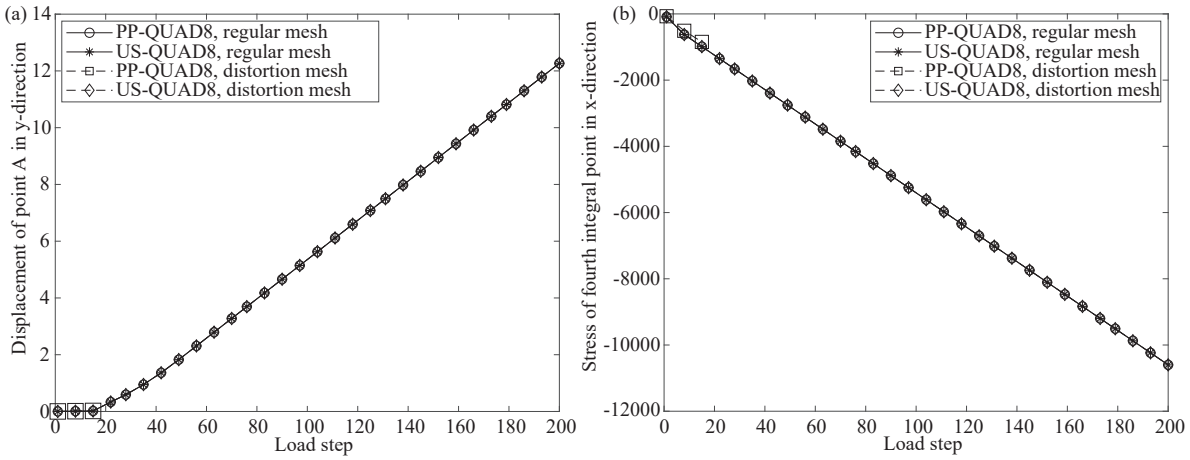

FIGURE 9 (a) Curves of vertical displacement at point A and (b) σ_{xx} stress at the fourth integration point in the first element versus the load step in cases of mixed distortion

3.2 | A cantilever beam with a shear load

The cantilever beam considered in section 3.1 is also used in this sub-section, but with a tip shear loading at the right end, as shown in Fig. 10. The shear force is obtained by applying equivalent nodal forces of 350 N, 2800 N and 350 N at pints (10, 0), (10,1) and (10, 2), respectively. The reaction shear force at the fixed end is represented by −350 N, −2800 N and −350 N at points (0, 0), (0,1) and (0, 2), respectively. Material parameters and beam sizes in this sub-section are given as $E = 6 \times 10^6$ Pa, $\upsilon = 0.25$, $\sigma_y = 1500$ Pa and $h = 60000$ Pa, length of the beam $l = 10$ m, width $w = 2$ m, depth $t = 2$ m. All the examples in this sub-section use the same material parameters. This problem involves cubic displacement field that increases the difficulty of getting exact solution. So neither US-QUAD8 nor PP-QUAD8 can be expected to reproduce exact solution because they are all quadratic elements. Nevertheless, we notice that the results for the four types of distortion given by US-QUAD8 element, are less sensitive to distortion as compared to the PP-QUAD8. In order to improve the performance of the two elements, 4×4 integration scheme is applied[42].

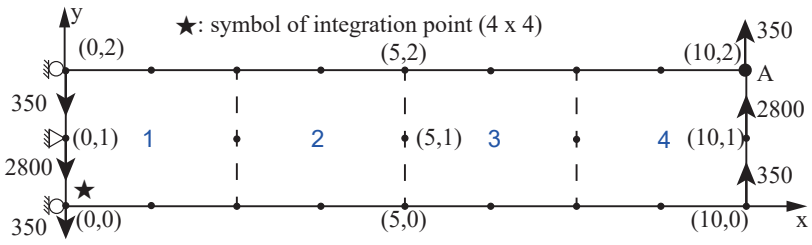

FIGURE 10 A tip-shear cantilever beam model with a regular mesh. Material parameters and beam sizes in this sub-section are given as $E = 6 \times 10^6$ Pa, $\upsilon = 0.25$, $\sigma_y = 1500$ Pa and $h = 60000$ Pa, length of the beam $l = 10$ m, width $w = 2$ m, depth $t = 2$ m, 4×4 Gaussian integration scheme is adopted.

For regular mesh, the contour plots of σ_{xx} stress and effective plastic strain are shown in Fig. 11. PP-QUAD8 and US-QUAD8 reproduce the same σ_{xx} stress and effective plastic strain when the mesh is regular. The maximum and minimum σ_{xx} stresses are 25756 Pa and −25756 Pa, respectively. The maximum and minimum effective plastic strains are 0.307 and 0.002, respectively.

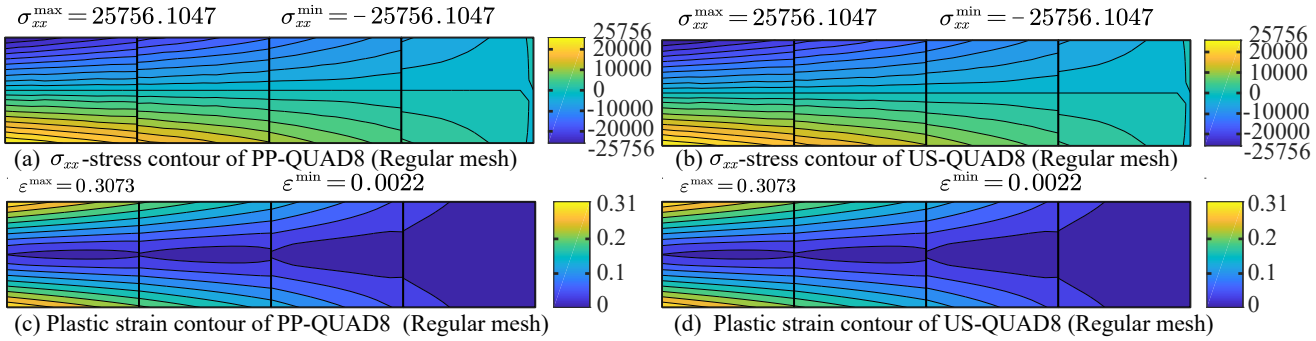

FIGURE 11 Contours of σ_{xx} stress and effective plastic strain for the tip-shear cantilever beam with regular mesh are plotted on the undeformed meshes

The curves of displacement at point A and the σ_{xx} stress at the first Gaussian integration point (see Fig. 10) in the first element are shown in Fig. 12. PP-QUAD8 and US-QUAD8 elements both produce the same results. The maximum vertical displacement 8.912 m and the maximum σ_{xx} stress 21978.691 Pa are considered as reference for the following comparisons.

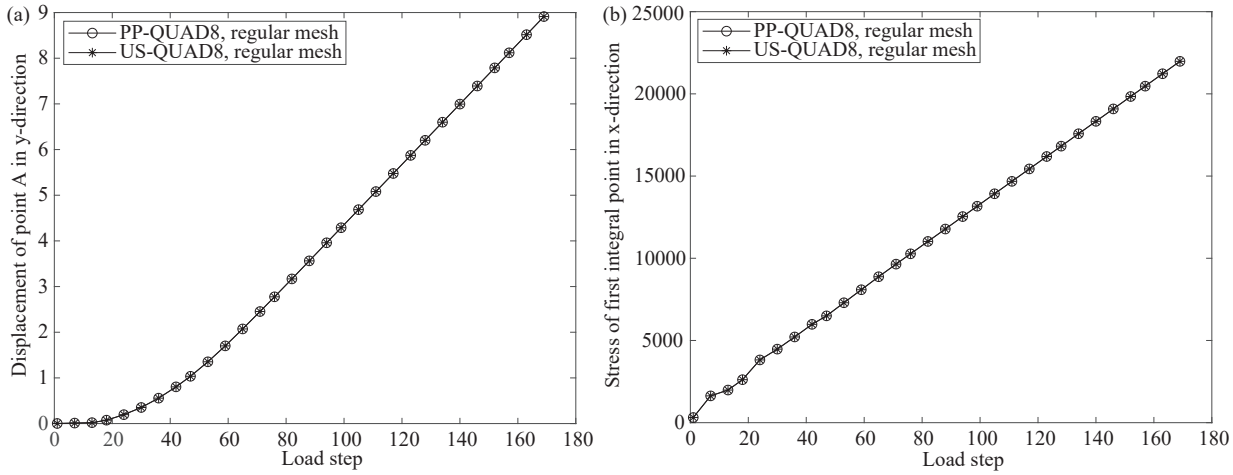

FIGURE 12 (a) Curves of vertical displacement at point A and (b) σ_{xx} stress at the first integration point in the first element versus the load step in cases of regular mesh

3.2.1 | Single distortion

The same meshes with angular distortion, curved-edge distortion and mid-side node distortion plotted in Fig. 5 are chosen in this example. From the contour plots in Fig. 13, PP-QUAD8 and US-QUAD8 both can not reproduce the same results obtained by regular mesh. However, the stresses produced by US-QUAD8 are better than PP-QUAD8 since the magnitudes of maximum and minimum σ_{xx} are closer to the references got by regular mesh. The relative maximum error of σ_{xx} stress is 22.800% by US-QUAD8 which is much smaller than 214.915% by PP-QUAD8 in case of angular distortion. Table 2 lists the relative errors of maximum σ_{xx} stress in the whole domain, displacement at point A in y direction and σ_{xx} stress at the first Gaussian point in the first element. The corresponding reference values are from those in case of regular mesh. From the contour plots in Figs. 13 (e) and (f), for curved-edge distortion, US-QUAD8 can reproduce very similar contour lines obtained in case of regular mesh while the results of PP-QUAD8 are poor. The σ_{xx} stress and effective plastic strain distributions of US-QUAD8 are relatively continuous and symmetric while the those of PP-QUAD8 are discontinuous and irregular. The maximum relative errors of σ_{xx}

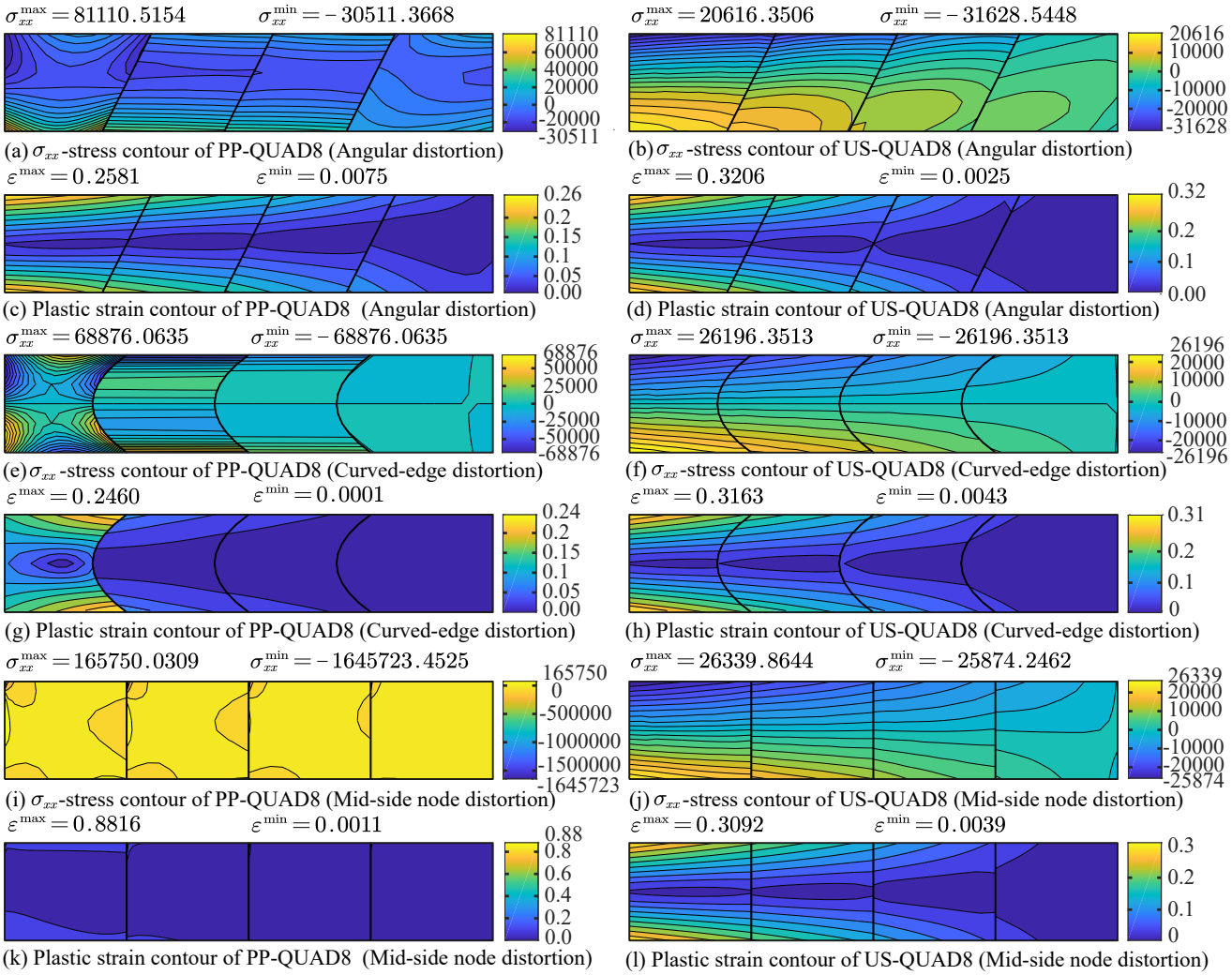

FIGURE 13 Contours of σ_{xx} stress and plastic strain for the tip-shear cantilever beam with angular distortion are plotted on the undeformed meshes

stress for PP-QUAD8 and US-QUAD8 are 167.416% and 1.709%, respectively. In case of the mid-side node distortion, the same conclusions can be obtained. The US-QUAD8 still shows better performance than PP-QUAD8 whether from the distributions of σ_{xx} stress and effective plastic strain, or the maximum relative errors. The maximum relative errors of σ_{xx} stress for PP-QUAD8 and US-QUAD8 are 6289.644% and 2.266%, respectively.

TABLE 2 Relative errors in case of tip shear example

Element type \ Distortion type	Angular distortion	Curved-edge distortion	Mid-side node distortion	Mixed distortion
PP-QUAD8 (σ_{xx})	214.915%	167.416%	6289.644%	432.715%
US-QUAD8 (σ_{xx})	**22.800%**	**1.709%**	**2.266%**	**10.436%**
PP-QUAD8 (U)	6.688%	51.114%	56.323%	50.377%
US-QUAD8 (U)	**1.516%**	**1.120%**	**0.595%**	**0.994%**
PP-QUAD8 (σ_{xx}^{gp})	132.743%	83.492%	280.015%	171.905%
US-QUAD8 (σ_{xx}^{gp})	**15.652%**	**0.439%**	**1.492%**	**1.863%**

U: the displacement at point A in y direction
σ_{xx}^{gp}: the stress at the first Gaussian point in the first element

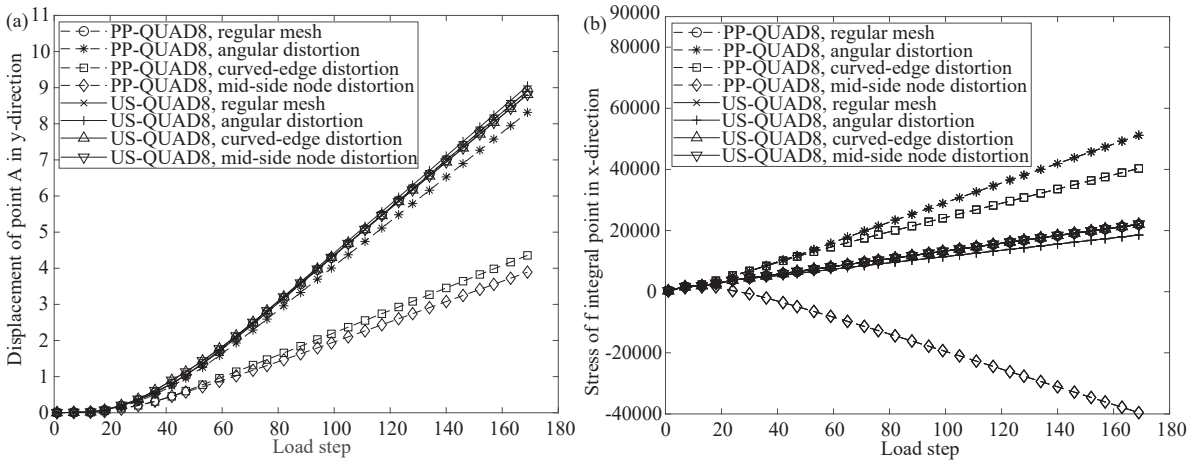

FIGURE 14 (a) Curves of vertical displacement at point A and (b) σ_{xx} stress at the first integration point in the first element versus the load step in cases of single distortion

As we can see from Fig. 14, as the increase of load step, the displacement and σ_{xx} stress at the first integration point of PP-QUAD8 deviate from the reference significantly, while those from US-QUAD8 coincide with the curves in case of regular mesh. The maximum vertical displacements for PP-QUAD8 are 8.316 m, 4.357 m and 3.893 m in cases of the angular distortion, curved-edge distortion and mid-side node distortion, respectively. Their relative errors reach 6.688%, 51.114% and 56.323% while US-QUAD8 only generates a little. The maximum vertical displacements for US-QUAD8 are 9.047 m, 8.813 m and 8.965 m which are comparable with those in case of regular mesh. The relative errors are both very small, 1.516%, 1.120% and 0.595%, respectively. It exhibits better performance of US-QUAD8. Similar conclusions can be drawn for the σ_{xx} stress at the integration point. PP-QUAD8 produces the maximum relative errors of 132.743%, 83.492% and 280.015%, respectively, while 15.652%, 0.439% and 1.492% for US-QUAD8.

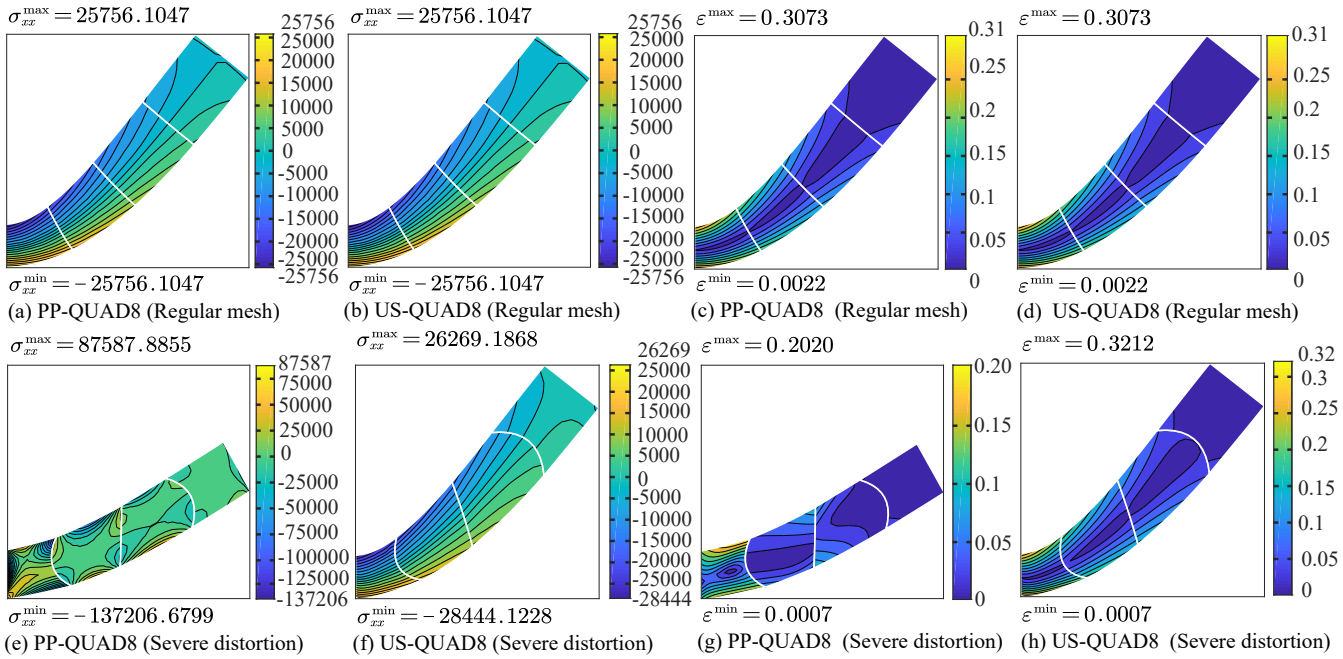

FIGURE 15 Contours of σ_{xx} stress for the tip-shear cantilever beam with mixed distortion are plotted on the deformed mesh

3.2.2 | Mixed distortion

We choose the mixed distorted mesh in Fig. 5(d) to test the mesh-distortion sensitivity of the present element. Under the meshes combining three typical distortions, US-QUAD8 reproduces much better σ_{xx} stress and effective plastic strain than PP-QUAD8, as shown in Fig. 15. The maximum relative errors of σ_{xx} stress for PP-QUAD8 and US-QUAD8 are 432.715% and 10.436%, respectively. In Fig. 16, the curves of displacement and σ_{xx} stress at integration point for PP-QUAD8 both deviate far away after entering into plastic stage. The maximum relative errors of displacement and σ_{xx} stress at Gaussian point for PP-QUAD8 are 50.377% and 171.905% while these for US-QUAD8 are 0.994% and 1.863%, respectively.

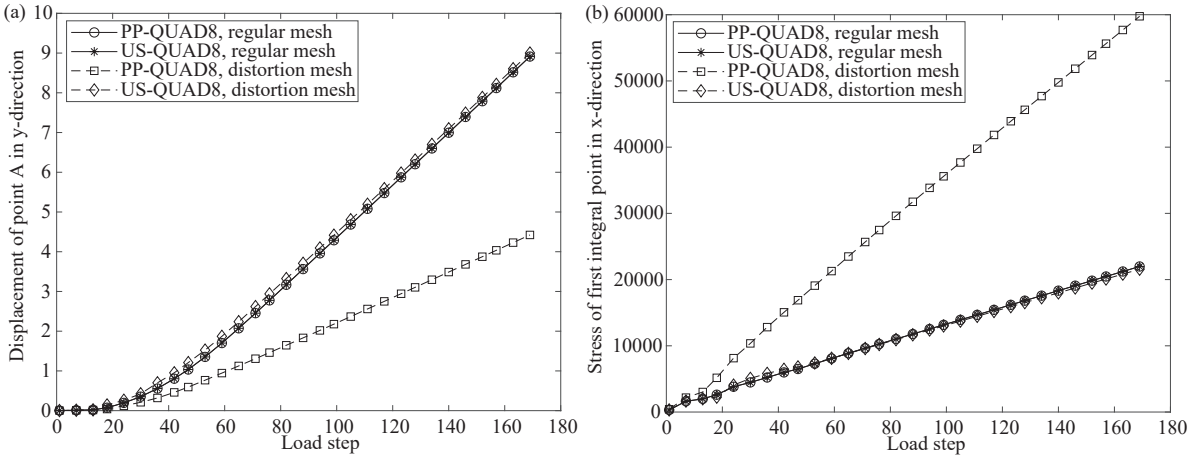

FIGURE 16 Curves of vertical displacement at point A and the σ_{xx} stress at the first integration point in the first element versus the load step in cases of mixed distortion

3.3 | CPU time comparison

Table 3 lists the computation time of the two elements under different distortion types for the tip moment example and tip shear example. 2×2 Gaussian integration scheme is adopted for tip moment example. Due to the higher order of displacement field involved, 4×4 Gaussian integration scheme is adopted for tip shear example. The specific information of the computer are as follows: CPU: i7-9700, memory: 16GB, system: Windows 10. The same maximum iteration number is taken in each load step. PP-QUAD8 element needs less computational time since extra calculation of metric shape function is required for US-QUAD8 element in case of regular mesh for the two problems. However, US-QUAD8 element takes less iteration numbers in cases of distorted mesh and shows better computational efficiency. Especially, PP-QUAD8 element cannot converge under mixed distorted situation. We also notice that US-QUAD8 element spends similar CPU time in each case of mesh distortion. For tip shear example, US-QUAD8 element takes less iteration numbers in cases of curved/mixed distorted mesh and shows much better computational efficiency. In the other two distortion types, the two elements take similar computational efforts. Again, we also observe that US-QUAD8 element spends similar CPU time in each case of mesh distortion.

TABLE 3 Computation time in case of tip moment and tip shear examples (Unit: second)

Element type \ Distortion type	Regular mesh	Angular distortion	Curved-edge distortion	Mid-side node distortion	Mixed distortion
PP-QUAD(tip-moment)	**7.5**	**10.6**	30.9	75.4	–
US-QUAD8(tip-moment)	12.1	12.3	**12.4**	**12.3**	**12.3**
PP-QUAD8(tip-shear)	**201.0**	**239.8**	2201.3	**291.8**	1479.1
US-QUAD8(tip-shear)	352.0	370.5	**384.4**	313.6	**353.9**

4 | CONCLUSIONS

The unsymmetric US-QUAD8 element is successfully extended to material non-linear analysis and shows excellent distortion immunity by comparing with the classical PP-QUAD8 element. Three typical distortions, namely angular distortion, curved-edge distortion and mid-side node distortion, as well as their combination are adopted to test the performance of US-QUAD8 element. Tip moment example where quadratic displacement field is involved exhibits good outcome of US-QUAD8 element that the displacement and stress agree well with each other both in regular and distorted meshes while PP-QUAD8 element produces poor results. The higher-order cubic displacement field involved tip shear example further verifies the excellent performance of US-QUAD8 element in large deformation analysis.

The encouraging results of the present work suggest that the unsymmetric element demonstrates better resistance to mesh distortion in material non-linear analysis. Therefore, our attention will focus on the application of the present element in the engineering problems with non-linear hyperelastic and anisotropic materials.

ACKNOWLEDGMENTS

J. Xu thanks the starting grant supported by Jiangsu university (Grant # 19JDG022). W. Chen thanks the National Natural Science Foundation of China (Grant # 51875263). W. Tu thanks the open fund of Hubei Key Laboratory of Mechanical Transmission and Manufacturing Engineering in Wuhan university of science and technology (Grant # 2017A03). S. Rajendran thanks the support provided by research grant no. RG 29/08 (M52050104) of Academic Research Fund (AcRF) Tier 1, Ministry of Education, Singapore for carrying out this research.

Author contributions

J. Xu and S. Rajendran conceived and planned the presented idea. J. Xu, X. Chen, W. Chen and S. Rajendran developed the theory. X. Chen and J. Xu contributed to the code programming and performed the computations. J. Xu, X. Chen, W. Chen, W. Tu and S. Rajendran contributed to the interpretation of the results. X. Chen, J. Xu and W. Tu took the lead in writing the manuscript. J. Xu, X. Chen, J. Lu and S. Rajendran worked on the revision. All authors provided critical feedback and helped shape the research, analysis and manuscript.

Financial disclosure

None reported.

Conflict of interest

The authors declare no potential conflict of interests.

Data availability statement

The data that support the findings of this study are available from the corresponding author upon reasonable request.

References

1. Zienkiewicz OC, Taylor RL, Zhu JZ. *The finite element method: its basis and fundamentals (seventh edition)*. Londan, UK: Butterworth-Heinemann . 2013.

2. Bathe KJ. *Finite Element Procedures. 2nd ed.* Upper Saddle River, New Jersey, USA: Prentice Hall . 2014.

3. Long YQ, Cen S, Long ZF. *Advanced Finite Element Method in Structural Engineering*. Berlin, Germany: Springer-Verlag, Tsinghua University Press . 2009.

4. Gifford LN. More on distorted isoparametric elements. *Int J Numer Meth Engng* 1979; 14(2): 290-291.

5. Kilicaslan C. Modelling and simulation of metal cutting by finite element method. Master's thesis. Izmir Institute of Technology. Izmir,Turkey: 2009.

6. Huang T, Yuan Y, Zheng J, Avital E, Wen P. Large deformations of tapered beam with finite integration method. *Engng Anal Bound Elem* 2019; 107: 115-123.

7. Soliman HA, Shash AY, El Hossainy TM, Abd-Rabou M. Investigation of process parameters in orthogonal cutting using finite element approaches. *Heliyon* 2020; 6(11): e05498.

8. Rajendran S, Zhang B. A FE-meshfree QUAD4 element based on partition of unity. *Comput Meth Appl Mech Eng* 2020; 197(1-4): 128-147.

9. Rajendran S, Zhang B, Liew KM. A partition of unity-based FE-meshfree QUAD4 element for geometric non-linear analysis. *Int J Numer Meth Engng* 2010; 82(12): 1574-1608.

10. Xu J, Rajendran S. A partition-of-unity based FE-meshfree QUAD4 element with radial-polynomial basis functions for static analyses. *Comput Meth Appl Mech Eng* 2011; 200(47-48): 3309-3323.

11. Wieckowski Z. The material point method in large strain engineering problems. *Comput Meth Appl Mech Eng* 2004; 193(39-41): 4417-4438.

12. Zhang X, Chen Z, Liu Y. *The material point method: A continuum-based particle method for extreme loading cases*. Beijing , China: Academic Press . 2016.

13. Chen F, Chen R, Jiang B. The adaptive finite element material point method for simulation of projectiles penetrating into ballistic gelatin at high velocities. *Engng Anal Bound Elem.* 2020; 117: 143-156.

14. Hughes TJ, Cottrell JA, Bazilevs Y. Isogeometric analysis: CAD, finite elements, NURBS, exact geometry and mesh refinement. *Comput Meth Appl Mech Eng* 2005; 194(39): 4135-4195.

15. Xu J, Vilanova G, Gomez H. A mathematical model coupling tumor growth and angiogenesis. *PLoS One* 2016; 53(39): 449-464.

16. Xu J, Vilanova G, Gomez H. Full-scale, three-dimensional simulation of early-stage tumor growth: The onset of malignancy. *Comput Meth Appl Mech Eng* 2016; 314: 126-146.

17. Xu J, Vilanova G, Gomez H. Phase-field model of vascular tumor growth: Three-dimensional geometry of the vascular network and integration with imaging data. *Comput Meth Appl Mech Eng* 2020; 359: 112648.

18. Liu Y, Sun L, Xu F, Liu Y, Cen Z. B spline-based method for 2-D large deformation analysis. *Engng Anal Bound Elem.* 2011; 35(5): 761-767.

19. Fried I. Accuracy of complex finite elements: I. Theory. *AIAA J* 1972; 10(3): 347-349.

20. Henshell R, Walters D, Warburton G. On possible loss of accuracy in curved finite elements. *J Sound Vibr* 1972; 23(4): 510-513.

21. Fried I. Possible loss of accuracy in curved (isoparametric) finite elements-comment on a paper by henshell, walters and warburton. *J Sound Vibr* 1972; 23(4): 507-510.

22. Stricklin J, Ho W, Richardson E, Haisler W. On isoparametric vs linear strain triangular elements. *Int J Numer Meth Engng* 1977; 11(6): 1041-1043.

23. Lee NS, Bathe KJ. Effects of element distortions on the performance of isoparametric elements. *Int J Numer Meth Engng* 1993; 36(20): 3553-3576.

24. Lautersztajn-S N, Samuelsson A. Further discussion on four-node isoparametric quadrilateral elements in plane bending. *Int J Numer Meth Engng* 2000; 47(1-3): 129-140.

25. Prathap G, Senthilkumar V, Manju S. Mesh distortion immunity of finite elements and the best-fit paradigm. *Sadhana* 2006; 31(5): 505-514.

26. Rajendran S, Liew KM. A novel unsymmetric 8-node plane element immune to mesh distortion under a quadratic displacement field. *Int J Numer Meth Engng* 2003; 58(11): 1713-1748.

27. Ooi ET, Rajendran S, Yeo JH. A 20-node hexahedron element with enhanced distortion tolerance. *Int J Numer Meth Engng* 2004; 60(15): 2501-2530.

28. Ooi ET, Rajendran S, Yeo JH. Extension of unsymmetric finite elements US-QUAD8 and US-HEXA20 for geometric nonlinear analyses. *Eng Comput* 2007; 24: 407-431.

29. Fu XR, Cen S, Li CF, Chen XM. Analytical trial function method for development of new 8-node plane element based on the variational principle containing Airy stress function. *Eng Comput* 2010; 27(4): 442-463.

30. Cen S, Zhou GH, Fu XR. A shape free 8-node plane element unsymmetric analytical trial function method. *Int J Numer Meth Engng* 2012; 91(2): 158-185.

31. Shang Y, Cen S, Zhou MJ. 8-node unsymmetric distortion-immune element based on Airy stress solutions for plane orthotropic problems. *Acta Mech* 2018; 229(12): 5031-5049.

32. Cen S, Zhou PL, Li CF, Wu CJ. An unsymmetric 4-node, 8-DOF plane membrane element perfectly breaking through MacNeal's theorem. *Int J Numer Meth Engng* 2015; 103(2): 469-500.

33. Li Z, Cen S, Wu CJ, Shang Y, Li CF. High-performance geometric nonlinear analysis with the unsymmetric 4-node, 8-DOF plane element US-ATFQ4. *Int J Numer Meth Engng* 2018; 114(9): 931-954.

34. Zhou PL, Cen S, Huang JB, Li CF, Zhang Q. An unsymmetric 8-node hexahedral element with high distortion tolerance. *Int J Numer Meth Engng* 2016; 109(8): 1130-1158.

35. Huang JB, Cen S, Li Z, Li CF. An unsymmetric 8-node hexahedral solid-shell element with high distortion tolerance: Linear formulations. *Int J Numer Meth Engng* 2018; 116(12-13): 759-783.

36. Li Z, Huang JB, Cen S, Li CF. An unsymmetric 8-node hexahedral solid-shell element with high distortion tolerance: Geometric nonlinear formulations. *Int J Numer Meth Engng* 2019; 114(9): 1130-1158.

37. Shang Y, Cen S, Qian ZH, Li CF. High-performance unsymmetric 3-node triangular membrane element with drilling DOFs can correctly undertake in-plane moments. *Eng Comput* 2018; 35(7): 2543-2556.

38. Shang Y, Ouyang W. 4-node unsymmetric quadrilateral membrane element with drilling DOFs insensitive to severe mesh-distortion. *Int J Numer Meth Engng* 2018; 113(10): 1589-1606.

39. Cen S, Shang Y, Zhou PL, et al. Advances in shape-free finite element methods: A review. *Eng Mech* 2017; 34: 1-14.

40. Cen S, Wu CJ, Li Z, Shang Y, Li CF. Some advances in high-performance finite element methods. *Eng Comput* 2019; 36: 2811-2834.

41. Li Z, Cen S, Huang JB, Li CF. Hyperelastic finite deformation analysis with the unsymmetric finite element method containing homogeneous solutions of linear elasticity. *International Journal for Numerical Methods in Engineering* 2020; 121(16): 3702–3721.

42. Rajendran S. A technique to develop mesh-distortion immune finite elements. *Comput Meth Appl Mech Eng* 2010; 199(17-20): 1044-1063.

43. Reddy JN. *An introduction to nonlinear finite element analysis*. Oxford University Press . 2004.

44. Dunne , Fionn . *Introduction to computational plasticity*. Oxford University Press . 2005.

How to cite this article: X. Chen, W. Chen, J. Xu, W. Tu, S. Rajendran, and J. Lu (xxxx), An unsymmetric 8-node plane element immune to mesh distortion for linear isotropic hardening material, *Int J Numer Meth Engng*, *xxxx*.